

Multi-fidelity Statistical Emulation of Eclipsing Stellar Light Curves

Jack Naish

University of Cambridge
jrhn2@cam.ac.uk

Neela Maadhuree Aramandla

University of Cambridge
nma37@cam.ac.uk

Ann-Kristin Dagmar Balve

University of Cambridge
akdb3@cam.ac.uk

1 Introduction

The search for life beyond Earth has shaped our understanding of the universe and our place in it. At first, this understanding was based upon metaphysical principles. Ancient Greek philosophers' Geocentrism [31] placed Earth at the universe's centre. Later, beliefs evolved into the 13th-century Heliocentric model [32], with Earth orbiting the sun. This shift reflected a growing self-awareness of our own lack of knowledge, a theme echoed in Nicholas of Cusa's 1440 work, "*De Docta Ignorantia*"¹, claiming the *learned man was one aware of his own ignorance* [33].

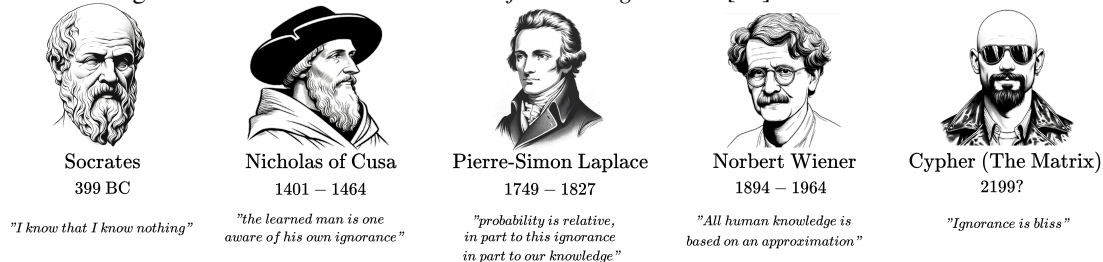


Figure 1: Ignorance through the Ages. Figurehead images generated by DALL-E 2
This theme has persisted throughout scientific advancements, from Kepler's Laws to Newton's theory of universal gravitation. Laplace, remarking on uncertainties in particle and planetary motion, attributed their trajectories *in part to this ignorance, in part to our knowledge* [2]. Norbert Wiener would agree, claiming *all human knowledge is based on an approximation* [20]. Today, quantification of ignorance underpins modern astrophysical models. We carry this idea forward into our study of distant exoplanets, part of the ongoing search for life beyond Earth.

2 Background

Exoplanets remain the subject of intense study since their first discovery in 1995. Yet, these celestial bodies often cannot be observed directly. When viewed from Earth, thousands of light years away, their reflected light is millions of times fainter than the host star [6]. One way astronomers circumvent this is by measuring transit events.

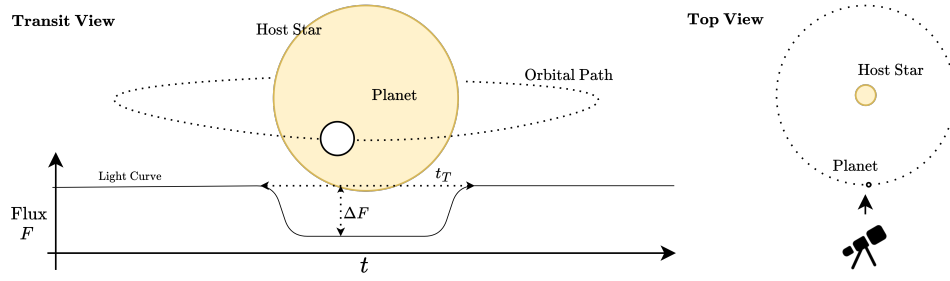


Figure 2: The transit method

As an exoplanet passes in front of its star, the apparent brightness is reduced. When observed over time, these transit events impose periodic dips in the resultant light curve (fig. 2). From this, orbital period, radius, and temperature can be derived. These help characterise the habitability of distant worlds [45] and often direct the science objectives of future space telescope missions [3].

¹On Learned Ignorance

2.1 Problem Statement

Despite technical advancements, accurately measuring exoplanet transit light curves through ground-based observations remains challenging. Continuous monitoring is often not possible due to Earth's rotation, variable weather conditions, and limited telescope availability. Consequently, light curves must be **interpolated** from a sparse brightness (flux) time-series [19].

Transit observations are also corrupted with **correlated noise** [18], often the result of complex astrophysical phenomena. Two primary generators of this noise are stellar variability and Earth's atmospheric turbulence. The former, driven by *sunspots*, *plages*, and *solar flares*, introduces quasi-periodic fluctuations onto light curve measurements [42]. The latter imposes scintillation and blurring on incoming starlight due to turbulent changes in atmospheric refractive indexes [34, 10].

2.2 Prior Works

As identified in a 2020 study [18], our ability to detect transits and infer their parameters depends on mitigating the effects of this correlated noise in flux measurements. A range of parametric models have been proposed for this purpose. These include wavelet [11] and Kalman filtering [21], harmonic decomposition [23], and sliding filter methods [30]. Although functional, these techniques ignore our ignorance; they lack systematic quantification of prediction uncertainty and don't allow prior knowledge encoding. Gaussian Processes (GPs) have recently emerged as a non-parametric alternative. Although historically limited to small time-series datasets by their cubic complexity, recent advances enable linear time matrix inversion by exploiting light curve structure [18]. Furthermore, GPs have been shown to outperform Deep Neural Networks in modelling transit light curves [19], leading to broad adoption amongst astronomers [28] [14] [16] [44].

In parallel to GPs, simulation remains a key tool when developing machine learning models for the physical world. However, existing approaches to light curve simulation have focused exclusively on high-fidelity techniques. These include computational fluid dynamics for turbulence [40] [39], magneto-hydrodynamics for solar wind modelling [29], and hydrodynamic simulation of solar flares [47]. There is a clear gap pertaining to the application of multifidelity modelling in this domain. Terabytes of historical observations from these astrophysical phenomena present an ideal setting to combine ideas of deep statistical emulation and multi-fidelity Gaussian Processes (MFGP), as an alternative to the status quo.

3 Method

Our proposed pipeline (fig. 3) first utilises an astrodynamics simulation to model ideal planetary transit events as viewed from Earth. By ideal, we mean theoretically accurate light curves uncorrupted by noise. Next, rather than simulating the underlying physics of stellar variability and turbulence-generating mechanisms, we capture their effects via statistically correct emulators, thus producing higher fidelity light curve estimates. The simulated astrodynamics data and emulated estimates are then combined into a multi-fidelity non-linear Gaussian process. This is where the demon of astrodynamical determinism meets the gremlin of stellar and turbulence uncertainty [25]. The MFGP is then deployed for interpolation of incomplete real-world light curve data, enabling accurate inference of transit duration, orbital period, and radius for distant solar systems. These inferred parameters can be combined with our understanding of planetary physics to help answer the question of exo-planet habitability.

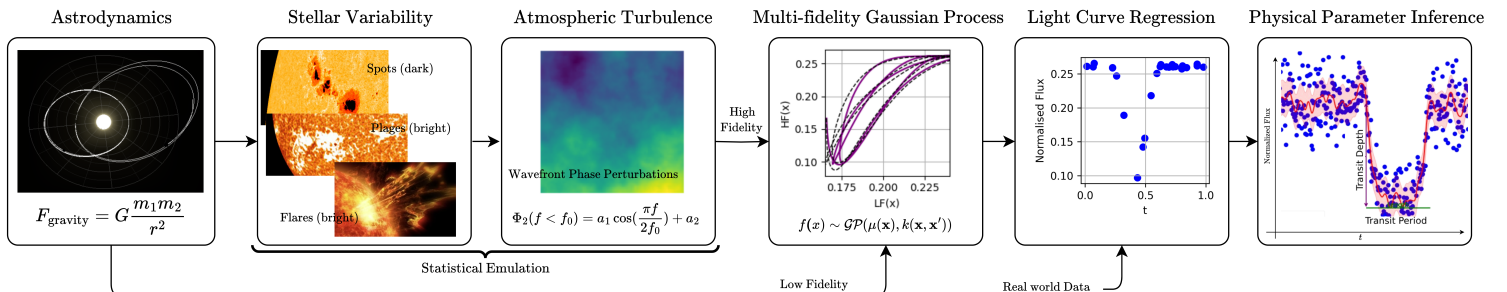


Figure 3: Overview of Methodology

3.1 Simulation: Astrodynamics

Our astrodynamics model simulates deterministic planetary motion by computing the net force on each celestial body. This force F_i results from the attraction between two masses m_i, m_j $i \neq j$, separated by distance r_{ij} as described by Newton's law of universal gravitation [49] eq. (1).

$$F_i = G \sum_{j=1, j \neq i}^N \frac{m_i m_j}{r_{ij}^2} \hat{r}_{ij} \quad (1) \quad a = \frac{F}{m} \quad (2) \quad v_i(t + \Delta t) = v_i(t) + a_i \Delta t \\ x_i(t + \Delta t) = x_i(t) + v_i(t) \Delta t \quad (3)$$

By resolving all forces on each body and dividing by planetary mass the resultant acceleration is obtained via Newton's second law eq. (2). The positions and velocities of the bodies are then updated via explicit Euler integration eq. (3) with time Δt :

To produce image sequences of exoplanet transit events as observed from Earth, we built a visualisation tool using THREE.js [15]. The User Interface (UI) includes controls for adjusting planetary parameters, such as mass, orbital velocity, perigee, and eccentricity. Additionally, stellar temperature, which heavily influences a star's visible spectrum emission, is calculated using an Hertzsprung-Russell (HR) diagram [13]. The resultant ideal light curve is plotted in realtime. An example 2-body system is shown by fig. 13.

3.2 Emulation: Atmospheric Turbulence

Light from our simulated celestial system can be represented as electromagnetic plane waves that propagate through outer space. In a vacuum, these waves travel without distortion. Upon reaching Earth, atmospheric turbulence affects air density and temperature causing refractive index to vary spatially over altitudes and temporally throughout transit events. As the speed of light is inversely proportional to its medium's refractive index (eq. (13)), starlight passing through these turbulent layers undergoes complex scintillation and blurring. This results in rapid brightness fluctuations that distort incoming light waveforms.

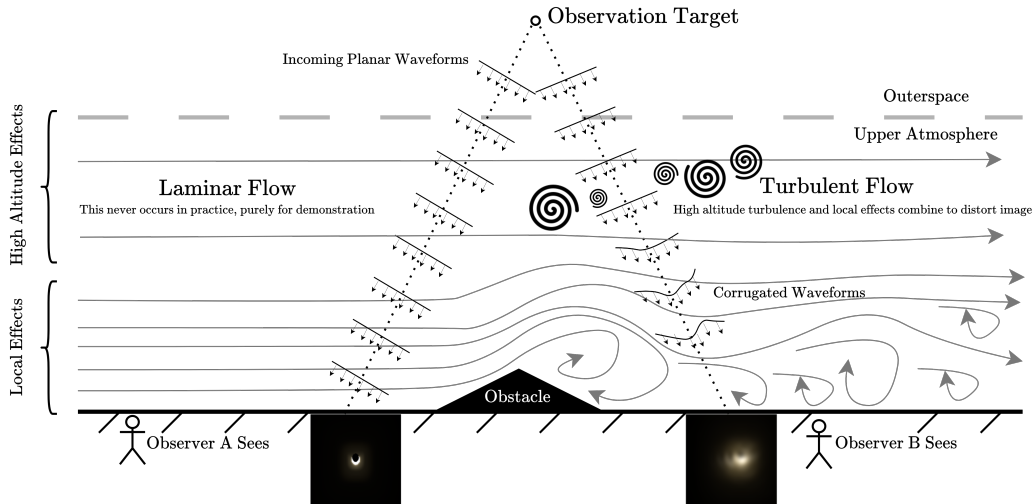


Figure 4: Effect of atmospheric turbulence on an incoming planar observation waveform

To capture and handle this noise source, we emulate *phase-screen generators* that mimic atmospheric turbulence's impact on light propagation. This method avoids the complexity of directly modelling the atmospheric conditions, which would require extensive Naiver Stokes computational fluid dynamics. By emulating the turbulence effects, we instead capture the '*gremlin of uncertainty*' ² without requiring explicit modelling of its underlying causes.

Our approach uses the Woofer-Tweener algorithm [10] to approximate the effects of turbulence on light. This involves decomposing the light spectra into two statistically independent signals: a high-frequency ('woofer') and low-frequency ('tweener') power spectra. By using complex Gaussian random numbers and Fourier transforms, we generate time sequences that replicate the effects of atmospheric turbulence on starlight. This technique, implemented in the Python library *MegaScreen* [1], allows us to study and capture the distorting effects of turbulence on celestial observations. Figure 5 shows an example applied to our own data ³

²the unpredictable and chaotic nature of turbulence

³the raw image is overly magnified for illustration purposes, in practice it would be a 'pinprick' of light).

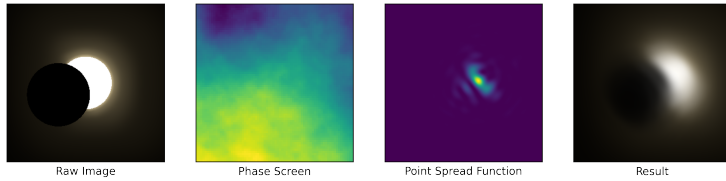


Figure 5: Enlarged image of planetary transit (left) produced by our aerodynamics simulation. Sampled wavefront phase screen and point spread function captures the effect of turbulence (middle). These, when convoluted with the raw image, produce an accurately distorted result (right).

3.3 Emulation: Stellar Variability

Stellar Variability causes fluctuations in a star’s normalised flux output (brightness) and is driven by *sun spots*, *plages*, and *flares*. Spots (fig. 6a) are darker, cooler surface regions formed by magnetic interaction with the star’s plasma [42], and which reduce flux emission. Plages (fig. 6b) are brighter, hotter, emit more energy, and increase the flux output. Flares (fig. 6c), resulting from intense magnetic energy bursts, create sporadic spikes in flux.

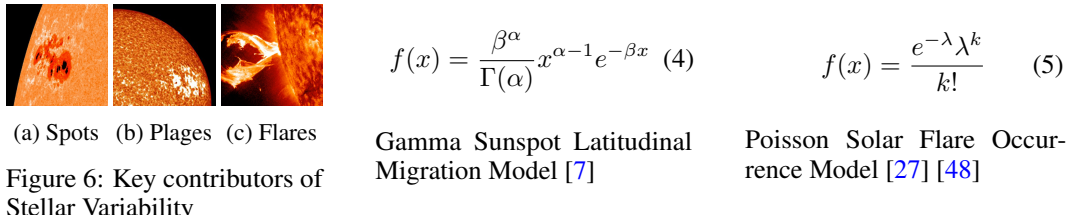


Figure 6: Key contributors of Stellar Variability

Gamma Sunspot Latitudinal Migration Model [7]

Poisson Solar Flare Occurrence Model [27] [48]

Empirical data (fig. 7) shows these phenomena exhibit decadal-scale (11.1 year) periodic trends in phase with the solar cycle. This can corrupt our light curve estimates since the only stellar flux changes we care about are those caused by a transiting exoplanet. In our case, rather than modeling the complex underlying physics of these variability-generating mechanisms, we capture their explicit realisation via statistically correct emulation based on historical observations.

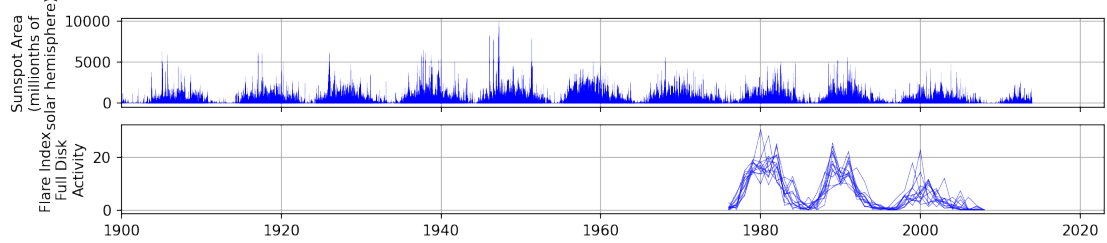


Figure 7: Historical records detailing Quasi-periodic stellar variability over decadal-scale solar cycles due to magnetically driven sunspot (top) [37] and flare (bottom) [12] activity. Data: *NASA/Marshall Solar Physics, National Geophysical Data Center*

Sun spots form at higher latitudes early in the cycle before migrating toward the solar equator due to differential rotation of the star. We adopt the model proposed by [7], which uses a Gamma Distribution (eq. (4)) to describe the sunspot group counts across latitudinal bands averaged over a solar cycle. *Flare* occurrences, on the other hand, are approximated using Poisson statistics (eq. (5)) in time and power-law statistics in size. Parameters are determined via maximum likelihood estimate from empirical flare data fig. 7 [48].

3.4 Gaussian Process Design

This section introduces kernel design and hyper-parameter optimisation of Gaussian processes, laying the groundwork for multifidelity GPs to follow.

3.4.1 Kernel Selection

Transiting light curves exhibit continuous, periodic trends. Prior knowledge of these characteristics can be encoded into our kernel function to improve performance. We initially apply simple RBF and Periodic kernels before combining their desirable characteristics via multiplicative compositions.

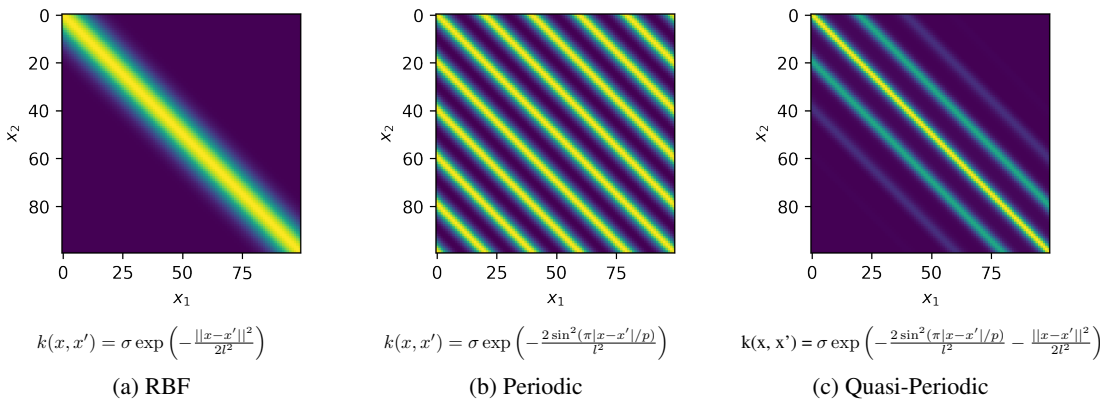


Figure 8: Different Kernel Functions analyzed

One of the most commonly used kernels is the RBF kernel that is parameterised by the length scale l and input distance r [19] (fig. 8a). Due to its simplicity in practice⁴ and easy interpretation⁵ it sets a good starting point as a baseline kernel. However, it can over-smooth functions resulting in poor models of the data [43] emphasizing the need to explore a wider set of kernels.

We test the Periodic kernel for modeling light curve data, leveraging its inherent capability to capture cyclical patterns in astronomical phenomena [46] (fig. 8b). This feature is particularly suitable for studying events like exoplanet transits, which are typically periodic under ideal conditions. While effective in modeling consistent periodicity, the kernel assumes a constant periodic behavior, which may not always align with varying nature in the astronomical data.

Another kernel commonly used in the astrophysics literature is the quasi-periodic (QP) kernel, obtained by taking the product of a squared exponential function and periodic term (the exponential of a sine-squared function) (fig. 8c). This kernel can accurately model quasi-periodic correlated noise in light curves [5] and samples drawn from a GP with QP-kernel have been shown to strongly resemble real light curves [38].

3.4.2 Gradient Ascent

Hyperparameter optimization is integral in our application of Gaussian Processes to analyze stellar light curves. Gradient ascent can facilitate this by iteratively updating the hyperparameters θ to maximize the log marginal likelihood eq. (6). Here, η is the learning rate, and ∇_{θ} represents the gradient with respect to the hyperparameters.

$$\boldsymbol{\theta}^{(t+1)} = \boldsymbol{\theta}^{(t)} + \eta \nabla_{\boldsymbol{\theta}} \log p(\mathbf{y} | \mathbf{X}, \boldsymbol{\theta}^{(t)}) \quad (6)$$

To optimise log marginal likelihood, we compute the partial derivatives of the kernel function with respect to its hyperparameters (see appendix, section 5.5). The gradient of the log marginal likelihood with respect to a hyperparameter θ_j is given by:

$$\frac{\partial}{\partial \theta_i} \log p(\mathbf{y}|\mathbf{X}, \boldsymbol{\theta}) = -\frac{1}{2} \text{Tr} \left(K^{-1} \frac{\partial K}{\partial \theta_i} \right) + \frac{1}{2} \mathbf{y}^\top K^{-1} \frac{\partial K}{\partial \theta_i} K^{-1} \mathbf{y} = \frac{1}{2} \text{tr}((\alpha \alpha^T - K^{-1}) \frac{\partial K}{\partial \theta_i}) \quad (7)$$

where $\frac{\partial K}{\partial \theta_i}$ is the partial derivative of the covariance matrix with respect to the hyperparameter θ_j .

Given the short and long period modes of stellar light curves, there are often many different, yet sub-optimal, ways to fit our GP. When optimizing the QP kernel hyperparameters and plotting a slice of our log-marginal-likelihood hyperplane as a function of its four dimensional hyperparameters, we observed it was fraught with local optima, wherein gradient ascent would get stuck. This made gradient ascent highly sensitive to its initial conditions, often requiring much trial and error. Furthermore, asymmetric learning rates⁶ often had to be manually tuned due to the variable magnitudes of different kernel hyperparameters.

3.4.3 Particle Swarm Optimisation

Motivated by naive gradient ascent's shortcomings, and the tedium of partial derivative computation, we pivoted our search algorithm to Particle Swarm Optimization [22]. PSO instead updates a group of particles, each representing a hyperparameter solution, iteratively based on two key components:

⁴It has relatively few hyperparameters to optimise.

⁵closer data points are more correlated

⁶using different learning rates for each hyperparameter dimension

the particle's best-known position ($pbest_i$) and the global best-known position ($gbest$) discovered by the swarm. The particle position $x_i^{(t+1)}$ and velocity $v_i^{(t+1)}$ update mechanism, devoid of gradients, is governed by:

$$\begin{aligned} v_i^{(t+1)} &= w \cdot v_i^{(t)} + c_1 \cdot r_1 \cdot (pbest_i - x_i^{(t)}) + c_2 \cdot r_2 \cdot (gbest - x_i^{(t)}) \\ x_i^{(t+1)} &= x_i^{(t)} + v_i^{(t+1)} \end{aligned}$$

Exploitation is codified in the above relation via social c_1 and cognitive c_2 coefficients which influence each particle's movement based on personal and swarm experiences. Random factors r_1 and r_2 introduce stochasticity, critical in facilitating exploitation. This explore-exploit dynamic led to drastic improvement over gradient ascent, as we'll see in section 4

3.5 Multi fidelity Modelling

In this section we apply principled methods to combine our simulation and emulation results through multifidelity modeling. This allows enhancement of our simple low cost astrodynamics data by injecting a small set of high-fidelity observations from our statistical emulators. Exploiting cross correlations between the low and high-fidelity data can lead to significant computational gains [36]. This technique affords us a richness of training data otherwise impossible to obtain through sole reliance on computationally demanding high-fidelity models [36].

Following the structure in [36], we have $S = 3$ fidelity sources which produce flux measurements $y_s(\mathbf{x}_t)$ at times $\mathbf{x}_t \in D_s \subseteq \mathcal{R}$. We order our time-flux tuples by increasing fidelity, s , as $\mathcal{D}_s = \{\mathbf{x}_s, \mathbf{y}_s\}$ such that:

- $D_1 = \{\mathbf{x}_1, \mathbf{y}_1\}$: astrodynamics (*low fidelity*)
- $D_2 = \{\mathbf{x}_2, \mathbf{y}_2\}$: astrodynamics + stellar variability. (*medium fidelity*)
- $D_3 = \{\mathbf{x}_3, \mathbf{y}_3\}$: astrodynamics + stellar variability + atmospheric turbulence. (*high fidelity*)

Note, D_1 is observed without error since our astrodynamics model is deterministic.

Using this data, we applied the *non-linear multifidelity model* (NLMFM) discussed in lectures [26]. NLMFM (eq. (8)) is an auto-regressive scheme where f_{s-1} and f_s are GPs modelling the data at fidelity level $s-1$ and s respectively. As a generalisation on its linear predecessor, NLMFM replaces the linear parameter $\rho \in \mathcal{R}$ with an unknown function z_{s-1} that learns a mapping between low and high fidelity outputs. $\delta_s(x_t) \sim \mathcal{GP}(\delta_s | \mu_{\delta_s}, k_s(x_s, x'_s))$ is a stationary GP representing how the low fidelity differs in practice, parameterised by mean μ_δ and covariance k_s .

$$f_1(x) = z_{s-1}(f_{s-1}(x)) + \delta_t(x) \quad (8)$$

Importantly, in our setup, each level of fidelity s containing our design points D_1, D_2, D_3 follows a nested structure, such that $D_s \subseteq D_{s-1}$. This imposes conditional independence on each $\delta_s(\cdot)$ therefore implying each fidelity s depends only on f_s, \dots, f_{s-1} through f_{s-1} . This, often termed the *Markov Property* [36, pg 3], is significant. It lets us eliminate model parameters across fidelity levels. It tells us we can learn nothing more about a given point $f_{t-1}(x)$ from any other model output $f_{s-1}(x')$, for $x \neq x'$ [36, pg 3]. And it lets us decouple the inference problem into s standard GP regression problems.

[36] proposes Bayesian non-parametric treatment of z by giving it a GP prior. The functional composition of the two GP priors ($z_{s-1}(f_{s-1}(x))$) produces a so called deep GP. Critically, this lets us capture non-linear, non-Gaussian relationships across varying stellar variability and turbulence fidelities. In practice, to avoid intractable variational approximations, the GP prior of each fidelity is set equal to the GP posterior from the previous inference level f_{s-1} .

3.6 Physical Parameter Estimation of Real Light Curve Data

In addition to the simulated data, the three real light curves HAT-P-16-b [9], HAT-P8-b [24], and HAT-P-21 b [8], obtained from the NASA Exoplanet Archive, have been used to fit GPs using the celerite2 [17] Python framework ⁷ and obtain the transit parameters **transit_depth**, and **transit_length**, and the planetary parameters **planet_radius**, and **orbital_radius**. The latter two can be inferred if physical properties of the exo-sun are known.

Assumptions To derive the planetary parameters from the light curves, several assumptions are made for simplifying the calculations:

1. Planets have a circular orbit around their sun. ⁸

⁷Celerite calculates GPs in a scalable and efficient way and is therefore preferred when dealing with large datasets (see section 5.8 for more details)

⁸This often holds for planets orbiting close to their stars.

2. The mass of the planet is much smaller than the mass of the sun. $M_p \ll M_\star$
3. The light curve originates from a 2-body system⁹ with a single star.

To infer **Transit_depth** δ_F (the flux change (%) during the transit), the difference between the baseline light flux outside of the transit $F_{\text{notransit}}$ and minimum flux during the transit event F_{transit} is taken and multiplied by 100 to obtain a percentage (eq. (9)). **Transit_length** T_{14} is the time duration a planet partially or fully transits in front of its star and is defined as the difference between the ingress and egress time. A detailed calculation can be accessed in the section 5.6.

$$\delta_F = \frac{F_{\text{notransit}} - F_{\text{transit}}}{F_{\text{notransit}}} \times 100 \quad (9) \quad T_{14} = T_{\text{egress}} - T_{\text{ingress}} \quad (10)$$

Once the transit depth is known, the **planetary_radius** R_p can be inferred if the solar radius R_{star} is known using eq. (11). Since planetary radius is traditionally in Jupyter units while solar radius is in Sun units, the end result has to be multiplied by the star to Jupyter ratio ($JP \approx 9.731$) to obtain the planetary radius is in Jupyter units. Finally, the **orbital_radius** a (the distance of an exoplanet from its star (eq. (12)) is calculated in astronomical units (AU)¹⁰ by a modified version of Kepler's law using the orbital period in years T and the solar mass in solar units M_\star .

$$R_p = R_{\text{star}} \sqrt{\delta_F} \times 9.731 \quad (11) \quad a = (M_\star \times T^2)^{1/3} \quad (12)$$

In addition to the parameter point estimates, the GP mean $\mu(x) = \hat{y}$ and standard deviation $\sigma(x)$ was utilised to compute the 95% **parameter uncertainty estimates** $CI(\hat{y}) = [\hat{y} - 1.96 \times \sigma(x), \hat{y} + 1.96 \times \sigma(x)]$. The absolute parameter estimate difference between the upper and lower bounds and the mean estimate was then calculated to obtain a measure of uncertainty. To finally compare the parameter estimates with the true values, the squared **error** ϵ^2 was used to quantify the accuracy of the inferred parameters $\epsilon^2 = (\hat{\theta} - \theta)^2$.

4 Results and Discussion

This section characterises the end-to-end performance of our multi-fidelity emulation and Gaussian Process pipeline (fig. 3). We first select a known exoplanet, HAT P-8-B, with light curve in fig. 9 (top). The astrophysical configuration of this system, parameterised by orbital eccentricity, radii, occlusion ratio, and mass, is replicated in our dynamics simulation from section 3.1. This produces a low-fidelity, ideal light curve (fig. 9 middle, blue line). On this, statistically emulated atmospheric turbulence is imposed, producing diffracted, scintillated transit event images (fig. 9 middle, red line & inset images). Finally, stellar variability effects are added, yielding the high fidelity light curve (fig. 9 middle, green line).

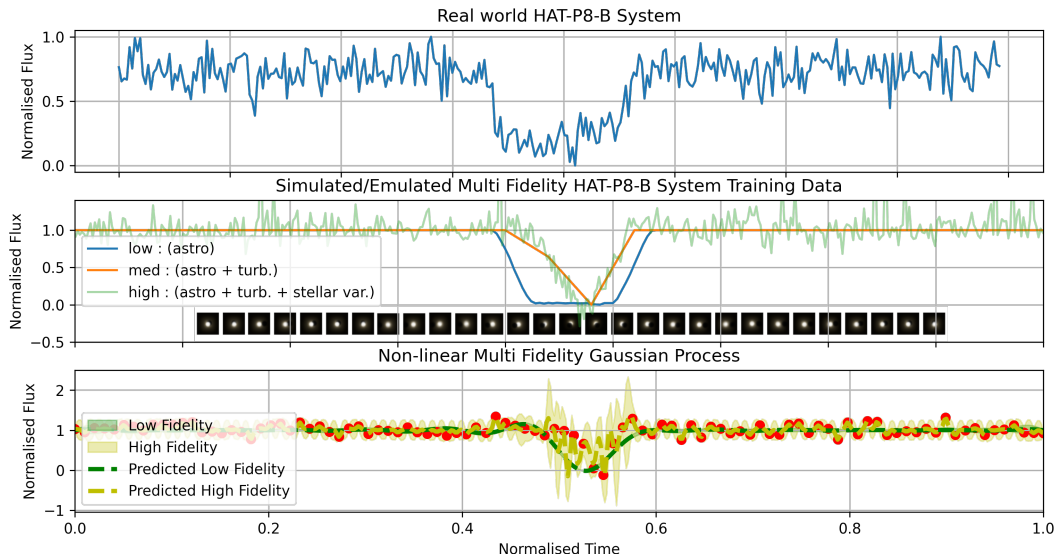


Figure 9: Real world Hat-P-8-B system (top) and its simulated/emulated counterpart (middle) with low, medium, and high fidelity light curves. Multifidelity Gaussian process (bottom) trained on simulated/emulated version of HAT-P-8-B

A multifidelity Gaussian Process is then fitted to this data using the Emukit framework [35] under an RBF kernel. Figure 9's bottom panel is key, showing the Gaussian process has learned cross-fidelity

⁹A single planet's transit around it's sun

¹⁰One astronomical unit of length is approximately equal to the distance from Sun to Earth

relationships and is effectively using lower-fidelity data to make accurate predictions at higher fidelity levels. This claim is supported by the strong similarities exhibited by the learned HF-LF correlation plot (fig. 14). Although out of scope, the error bars of the high-fidelity curve could be combined with a acquisition function to tell astronomers at what times they should next make an observation.

Figure 10 demonstrates fitting GPs (RBF, Periodic, QP) on the low fidelity simulated HAT-P-8-B curve using different kernels before (top) and after (bottom) hyperparameter optimisation. Initially, all GPs exhibit large residuals between predictive means (blue line) and data (green dots). After applying hyperparameter optimisation via gradient ascent and PSO separately, GP residuals are reduced and log marginal likelihood (LML) increased. The LML surface (middle row) shows the start point in hyperparameter space before optimisation (black star) and the final solution obtained via gradient ascent (white plus) and PSO (white cross). For periodic and QP kernels, we observed gradient ascent was very sensitive to initial condition and often became stuck in local optima. This happens because it can only move in the direction of ascent. Conversely, PSO circumvents this problem by combining individual particle knowledge with the global best position collectively known by the swarm to ‘jump’ out of local optima.

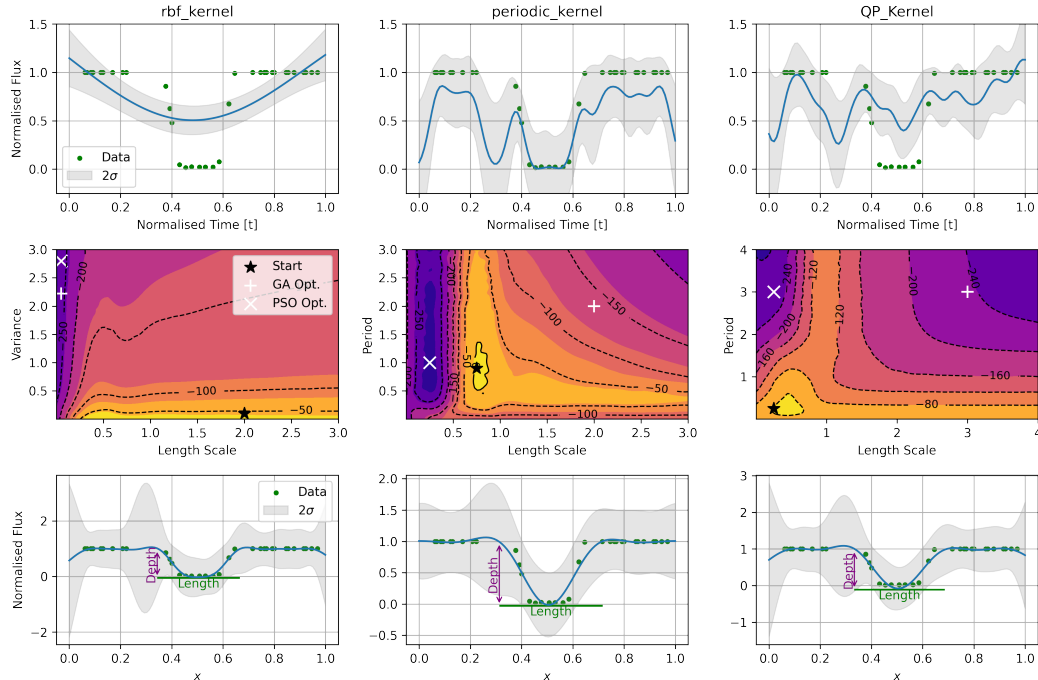


Figure 10: RBF, Periodic, and Quasi-periodic Gaussian Process kernels before (top) and after (bottom) hyperparameter optimisation.

4.1 Light Curve Interpolation

In addition to the synthetic HAT-P8-B datasets explored above, we deploy our Gaussian Processes onto the equivalent real-world light curves (fig. 11) using light curve data and parameter values from the NASA Exoplanet archive [4]. Informed by our previous kernel and hyperparameter experiment, PSO and the QP-Kernel were used.

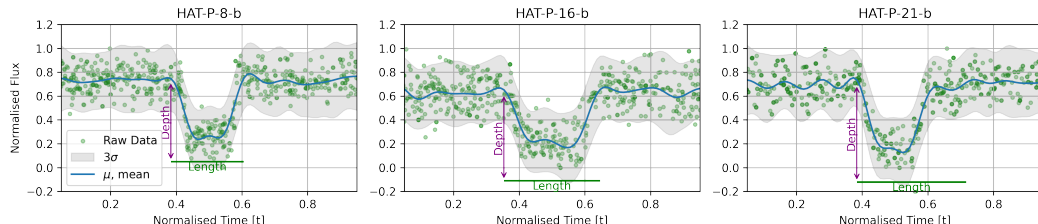


Figure 11: Gaussian Process fitted to real world data demonstrating interpolation and parameter estimation of transit depth and length

4.2 Parameter Estimation

Our results show that fitting GPs on real transit light curves allows us to accurately infer transit and physical parameters within reasonable confidence intervals. While the transit depth is overall reliably predicted across all three planets, transit length is less confidently predicted as visible by the larger 95% confidence intervals. These two measurements, combined with equations from section 3.6 allow us to infer planetary data as tabulated in fig. 12. Besides slightly off estimates for planetary radius for HAT-P-8-b, the other exo-planetary and orbital radius parameters were accurately inferred.

Figure 12: Parameter Estimates for three real exoplanets

(a) Parameter Estimates HAT-P-8 b				(b) Parameter Estimates HAT-P-16 b			
Parameter	Real Value	Predicted Value	MSE	Parameter	Real Value	Predicted Value	MSE
Solar Mass	1.2800 +/- 0.0400	-	-	Solar Mass	1.2180 +/- 0.0390	-	-
Solar Radius	1.5800 +/- 0.0800	-	-	Solar Radius	1.2370 +/- 0.0540	-	-
Orbital Period	3.0763 +/- 0.0000	-	-	Orbital Period	2.7760 +/- 0.0000	-	-
Transit Depth	0.0090 +/- 0.0002	0.0103 +/- 0.0008	0.000002	Transit Depth	0.0115 +/- 0.0000	0.0115 +/- 0.0011	0.000000
Transit Length	0.1587 +/- 0.0011	0.1699 +/- 0.1368	0.000126	Transit Length	0.1276 +/- 0.0013	0.1410 +/- 0.3486	0.000179
Planet Radius	1.5000 +/- 0.0800	1.4606 +/- 0.1371	0.001549	Planet Radius	1.2890 +/- 0.0660	1.2892 +/- 0.1177	0.000000
Orbital Radius	0.0487 +/- 0.0026	0.0449 +/- 0.0005	0.000014	Orbital Radius	0.0413 +/- 0.0004	0.0413 +/- 0.0004	0.000000

(c) Parameter Estimates HAT-P-21 b			
Parameter	Real Value	Predicted Value	MSE
Solar Mass	0.9470 +/- 0.0420	-	-
Solar Radius	1.1050 +/- 0.0440	-	-
Orbital Period	4.1245 +/- 0.0000	-	-
Transit Depth	0.0090 +/- 0.0001	0.0098 +/- 0.0016	0.000001
Transit Length	0.1530 +/- 0.0027	0.1611 +/- 0.3347	0.000066
Planet Radius	1.0240 +/- 0.0520	1.0215 +/- 0.1342	0.000006
Orbital Radius	0.0498 +/- 0.0007	0.0494 +/- 0.0007	0.000000

5 Conclusion

5.1 Future Work

While our work shows the potential of NLMFMs for exoplanet light curve interpolation and data-efficient emulation, its application to transit forecasting, inspired by [19], remains unexplored. This could facilitate inference of additional exo-planetary parameters, such as orbital period, which require the observation of at least two transit events to be accurate.

Although we limited ourselves to three distinct multi-fidelity levels, this was in hindsight somewhat arbitrary. Future works could examine automatically decomposing correlated noise sources across n levels.

5.2 Closing Thoughts

Our team systematically investigated a practical application of machine learning in the physical world, namely eclipsing exoplanet light curves. We applied simulation, deep statistical emulation, multi fidelity models, and Gaussian Processes. Our chosen topic required extensive background reading on areas outside our comfort zone, such as heliophysics and turbulence models. This helped drive home our learning by applying familiar course content to an unfamiliar context.

References

- [1] Welcome to MegaScreen’s documentation! — MegaScreen 0.5 documentation. <https://megascreen.readthedocs.io/en/latest>, January 2021. [Online; accessed 14. Jan. 2024].
- [2] Laplace: Essay on probabilities. https://mathshistory.st-andrews.ac.uk/Extras/Laplace_Probabilities, March 2023. [Online; accessed 16. Jan. 2024].
- [3] ESA Science & Technology - The future of exoplanet research. <https://sci.esa.int/web/exoplanets/-/60657-the-future-of-exoplanet-research>, January 2024. [Online; accessed 16. Jan. 2024].
- [4] Exoplanet-catalog – Exoplanet Exploration: Planets Beyond our Solar System. <https://exoplanets.nasa.gov/exoplanet-catalog/1224/hat-p-8-b>, January 2024. [Online; accessed 18. Jan. 2024].

- [5] S Aigrain, F Pont, and S Zucker. A simple method to estimate radial velocity variations due to stellar activity using photometry. *Monthly notices of the royal astronomical society*, 419(4):3147–3158, 2012.
- [6] Aude Ekundayo Pauline Alapini Odunlade. *Transiting exoplanets: characterisation in the presence of stellar activity*. PhD thesis, University of Plymouth, England, UK, March 2010.
- [7] Ajimandiram Krishnankuttyair Amaranathan Sabarinath, Girija Puthumana Beena; Anil Kumar. Modelling the shape of sunspot cycle using a modified Maxwell-Boltzmann probability distribution function - ProQuest. January 2020.
- [8] GÁ Bakos, J Hartman, G Torres, David W Latham, Géza Kovács, Robert W Noyes, DA Fischer, JA Johnson, GW Marcy, AW Howard, et al. Hat-p-20b-hat-p-23b: Four massive transiting extrasolar planets. *The Astrophysical Journal*, 742(2):116, 2011.
- [9] LA Buchhave, GÁ Bakos, JD Hartman, G Torres, G Kovács, DW Latham, RW Noyes, GA Esquerdo, M Everett, AW Howard, et al. Hat-p-16b: A 4 mj planet transiting a bright star on an eccentric orbit. *The Astrophysical Journal*, 720(2):1118, 2010.
- [10] David F. Buscher. Simulating large atmospheric phase screens using a woofer-tweeter algorithm. *Opt. Express*, 24(20):23566–23571, October 2016.
- [11] Joshua A. Carter, Jennifer C. Yee, Jason Eastman, B. Scott Gaudi, and Joshua N. Winn. Analytic Approximations for Transit Light-Curve Observables, Uncertainties, and Covariances. *Astrophys. J.*, 689(1):499, December 2008.
- [12] National Geophysical Data Center. Solar Terrestrial Physics. *U.S. Department of Commerce*, June 2009.
- [13] Contributors to Wikimedia projects. Main sequence - Wikipedia, January 2024. [Online; accessed 14. Jan. 2024].
- [14] Stefano Covino, Marco Landoni, Angela Sandrinelli, and Aldo Treves. Looking at Blazar Light-curve Periodicities with Gaussian Processes. *Astrophys. J.*, 895(2):122, June 2020.
- [15] Brian Danchilla. Three.js Framework. In *Beginning WebGL for HTML5*, pages 173–203. Apress, Berkeley, CA, Berkeley, CA, USA, 2012.
- [16] Thomas M. Evans, Suzanne Aigrain, Neale Gibson, Joanna K. Barstow, David S. Amundsen, Pascal Tremblin, and Pierre Mourier. A uniform analysis of HD 209458b Spitzer/IRAC light curves with Gaussian process models. *Mon. Not. R. Astron. Soc.*, 451(1):680–694, July 2015.
- [17] Daniel Foreman-Mackey, Eric Agol, Sivaram Ambikasaran, and Ruth Angus. Fast and scalable Gaussian process modeling with applications to astronomical time series. *arXiv*, March 2017.
- [18] Tyler A. Gordon, Eric Agol, and Daniel Foreman-Mackey. A Fast, Two-dimensional Gaussian Process Method Based on Celerite: Applications to Transiting Exoplanet Discovery and Characterization. *Astron. J.*, 160(5):240, November 2020.
- [19] Imène R. Goumire, Alec M. Dunton, Amanda L. Muyskens, Benjamin W. Priest, and Robert E. Armstrong. Light curve completion and forecasting using fast and scalable Gaussian processes (MuyGPs). *arXiv*, August 2022.
- [20] Doug Hill. Norbert Wiener and the Counter-Tradition to the Dream of Mastery - IEEE Technology and Society. *IEEE Technology and Society*, February 2021.
- [21] Brandon C. Kelly, Andrew C. Becker, Małgorzata Sobolewska, Aneta Siemiginowska, and Phil Uttley. FLEXIBLE AND SCALABLE METHODS FOR QUANTIFYING STOCHASTIC VARIABILITY IN THE ERA OF MASSIVE TIME-DOMAIN ASTRONOMICAL DATA SETS. *Astrophys. J.*, 788(1):33, May 2014.
- [22] J. Kennedy and R. Eberhart. Particle swarm optimization. In *Proceedings of ICNN'95 - International Conference on Neural Networks*, pages 1995–01. IEEE.
- [23] D. M. Kipping, J. Hartman, L. A. Buchhave, A. R. Schmitt, G. Á. Bakos, and D. Nesvorný. THE HUNT FOR EXOMOOONS WITH KEPLER (HEK). II. ANALYSIS OF SEVEN VIABLE SATELLITE-HOSTING PLANET CANDIDATES*. *Astrophys. J.*, 770(2):101, May 2013.
- [24] David W Latham, Gáspár Á Bakos, Guillermo Torres, Robert P Stefanik, Robert W Noyes, Géza Kovács, András Pál, Geoffrey W Marcy, Debra A Fischer, R Paul Butler, et al. Hatnet field g205: Follow-up observations of 28 transiting-planet candidates and confirmation of the planet hat-p-8b. *arXiv preprint arXiv:0812.1161*, 2008.

- [25] Neil D. Lawrence. Introduction: ML and the Physical World, October 2023. [Online; accessed 13. Jan. 2024].
- [26] Neil D. Lawrence. Multifidelity Modelling, November 2023. [Online; accessed 18. Jan. 2024].
- [27] Yuri E. Litvinenko and M. S. Wheatland. Modeling the Rate of Occurrence of Solar Flares. *Astrophys. J.*, 550(1):L109, March 2001.
- [28] Rodrigo Luger, Daniel Foreman-Mackey, and Christina Hedges. Mapping Stellar Surfaces. II. An Interpretable Gaussian Process Model for Light Curves. *Astron. J.*, 162(3):124, August 2021.
- [29] Eckart Marsch. Solar wind and kinetic heliophysics. *Ann. Geophys.*, 36(6):1607–1630, November 2018.
- [30] T. Mazeh and S. Faigler. Detection of the ellipsoidal and the relativistic beaming effects in the CoRoT-3 lightcurve. *Astron. Astrophys.*, 521:L59, October 2010.
- [31] The Editors Of Encyclopaedia Britannica. Geocentric model | Definition, History, & Facts. *Encyclopædia Britannica*, December 2023.
- [32] The Editors Of Encyclopaedia Britannica. Heliocentrism | Definition, History, & Facts. *Encyclopædia Britannica*, December 2023.
- [33] The Editors Of Encyclopaedia Britannica. Nicholas Of Cusa. *Encyclopædia Britannica*, December 2023.
- [34] J. Osborn, D. Föhring, V. S. Dhillon, and R. W. Wilson. Atmospheric scintillation in astronomical photometry. *Mon. Not. R. Astron. Soc.*, 452(2):1707–1716, September 2015.
- [35] Andrei Paleyes, Mark Pullin, Maren Mahsereci, Cliff McCollum, Neil D. Lawrence, and Javier Gonzalez. Emulation of physical processes with Emukit. *arXiv*, October 2021.
- [36] P. Perdikaris, M. Raissi, A. Damianou, N. D. Lawrence, and G. E. Karniadakis. Nonlinear information fusion algorithms for data-efficient multi-fidelity modelling. *Proc. R. Soc. A.*, 473(2198):20160751, February 2017.
- [37] NASA/Marshall Solar Physics. Royal Observatory, Greenwich - USAF/NOAA Sunspot Data. *Solar Physics*, March 2017.
- [38] Vinesh Rajpaul, Suzanne Aigrain, Michael A Osborne, Steven Reece, and S Roberts. A gaussian process framework for modelling stellar activity signals in radial velocity data. *Monthly Notices of the Royal Astronomical Society*, 452(3):2269–2291, 2015.
- [39] Subhajit Sarkar, Enzo Pascale, Andreas Papageorgiou, Luke J. Johnson, and Ingo Waldmann. ExoSim: the Exoplanet Observation Simulator. *Exp. Astron.*, 51(2):287–317, April 2021.
- [40] Wolfram Schmidt. *Numerical Modelling of Astrophysical Turbulence*. Springer International Publishing, Cham, Switzerland.
- [41] Sara Seager and Gabriela Mallen-Ornelas. A unique solution of planet and star parameters from an extrasolar planet transit light curve. *The Astrophysical Journal*, 585(2):1038, 2003.
- [42] Sami K. Solanki. Sunspots: An overview. *Astron. Astrophys. Rev.*, 11(2):153–286, April 2003.
- [43] Michael L Stein. *Interpolation of spatial data: some theory for kriging*. Springer Science & Business Media, 2012.
- [44] H. F. Stevance and A. Lee. What can Gaussian processes really tell us about supernova light curves? Consequences for Type II(b) morphologies and genealogies. *Mon. Not. R. Astron. Soc.*, 518(4):5741–5753, February 2023.
- [45] Tim Van Hoolst, Lena Noack, and Attilio Rivoldini. Exoplanet interiors and habitability. *Advances in Physics: X*, January 2019.
- [46] Yuyang Wang, Roni Khardon, and Pavlos Protopapas. Nonparametric bayesian estimation of periodic light curves. *The Astrophysical Journal*, 756(1):67, 2012.
- [47] Harry P. Warren. Multithread Hydrodynamic Modeling of a Solar Flare. *Astrophys. J.*, 637(1):522, January 2006.
- [48] M. S. Wheatland. A statistical solar flare forecast method. *Space Weather*, 3(7), July 2005.
- [49] Curtis A. Wilson. From kepler's laws, so-called, to universal gravitation: Empirical factors. *Archive for History of Exact Sciences*, 6(2):89–170, 1970.

Appendix

$$v = \frac{c}{r_n} \quad (13)$$

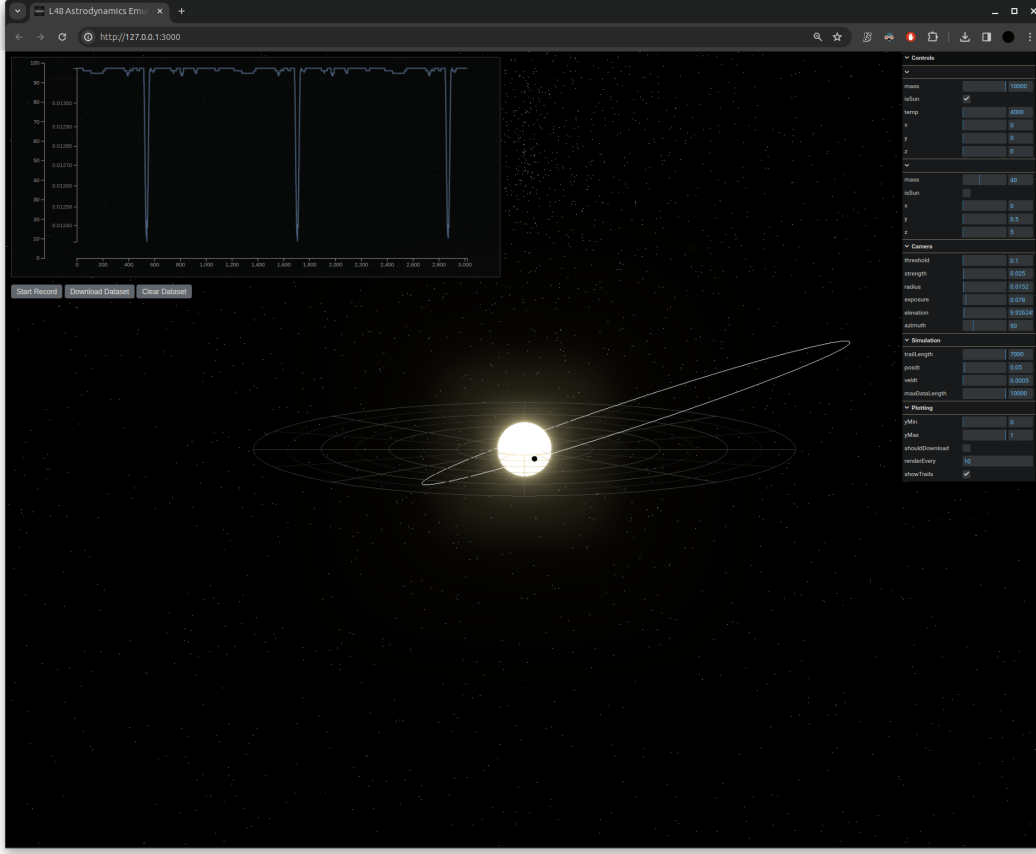


Figure 13: Astrodynamics simulation interface with controls for adjusting orbital system configuration. A demonstration two-body highly eccentric orbital system is shown with realtime light curve estimate plotted using d3.js.

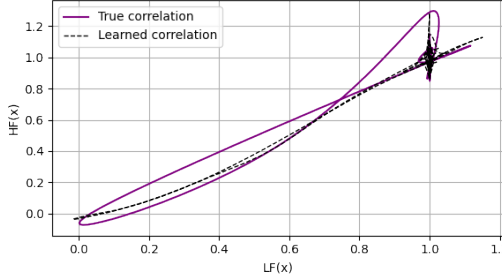


Figure 14: Low-high fidelity correlation of learned multi-fidelity GP

5.3 Detailed Calculations for the Emulation of the turbulence model

$$\Phi(f) = A[f^2 + F_0^2]^{-\frac{8}{6}} \quad (14)$$

where A scaling constant , frequency $F_0 \sim V/L_0$, f , velocity V , and turbulence lower scale L_0 [10]. The signal then decomposed into two statistically independent signals: a “woofer” and “tweener”, by loudspeaker analogy, representing high frequency and low frequency power spectrums respectively. a_1 and a_2 are continuity constants at crossover frequency f_0 . [10].

$$\Phi_1(f) = \Phi(f) - \Phi_2(f) \quad (15)$$

Tweener Signal Spectrum

$$\Phi_2(f < f_0) = a_1 \cos\left(\frac{\pi f}{2f_0}\right) + a_2 \quad (16)$$

Woofer Signal Spectrum

Complex Gaussian random numbers are independently sampled from woofer and tweener spectra. These are multiplied by the square root of the spectrum and Fourier transformed to give a time-sequence. The author's accompanying Python library *MegaScreen* [1] provides an implementation of this setup.

5.4 Marginal Likelihood

The log marginal likelihood of a GP, given data $\mathcal{D} = \{(\mathbf{x}_i, y_i)\}_{i=1}^N$, can be expressed as:

$$\log p(\mathbf{y}|\mathbf{X}, \boldsymbol{\theta}) = -\frac{1}{2}\mathbf{y}^\top K^{-1}\mathbf{y} - \frac{1}{2}\log|K| - \frac{N}{2}\log 2\pi \quad (17)$$

Here, \mathbf{y} is the vector of observations, \mathbf{X} represents the input matrix, K is the covariance matrix computed using a kernel function $k(\mathbf{x}, \mathbf{x}'; \boldsymbol{\theta})$ parameterized by hyperparameters $\boldsymbol{\theta}$, and N is the number of observations.

5.5 Gradient Ascent Partial Derivatives

This section details the manually computed partial derivatives for each of our kernel functions, used as part of our naive gradient ascent update routine.

Radial Basis Function (RBF) Kernel

$$k(x_i, x_j) = \sigma^2 \exp\left(-\frac{\|x_i - x_j\|^2}{2l^2}\right) \quad (18)$$

$$\frac{\partial k(x_i, x_j)}{\partial \sigma^2} = \exp\left(-\frac{\|x_i - x_j\|^2}{2l^2}\right) \quad (19)$$

$$\frac{\partial k(x_i, x_j)}{\partial l} = \sigma^2 \exp\left(-\frac{\|x_i - x_j\|^2}{2l^2}\right) \left(\frac{\|x_i - x_j\|^2}{l^3}\right) \quad (20)$$

Periodic Kernel

$$k(x_i, x_j) = \sigma^2 \exp\left(-\frac{2\sin^2\left(\frac{\pi}{P}|x_i - x_j|\right)}{l^2}\right) \quad (21)$$

$$\frac{\partial k(x_i, x_j)}{\partial \sigma^2} = \exp\left(-\frac{2\sin^2\left(\frac{\pi}{P}|x_i - x_j|\right)}{l^2}\right) \quad (22)$$

$$\frac{\partial k(x_i, x_j)}{\partial l} = \sigma^2 \exp\left(-\frac{2\sin^2\left(\frac{\pi}{P}|x_i - x_j|\right)}{l^2}\right) \left(\frac{4\sin^2\left(\frac{\pi}{P}|x_i - x_j|\right)}{l^3}\right) \quad (23)$$

$$\frac{\partial k(x_i, x_j)}{\partial P} = \sigma^2 \exp\left(-\frac{2\sin^2\left(\frac{\pi}{P}|x_i - x_j|\right)}{l^2}\right) \left(\frac{4\pi|x_i - x_j| \sin\left(\frac{\pi}{P}|x_i - x_j|\right) \cos\left(\frac{\pi}{P}|x_i - x_j|\right)}{P^2 l^2}\right) \quad (24)$$

Quasi-periodic Kernel:

$$k(x_i, x_j) = \sigma \exp\left(-\frac{2\sin^2(\pi|x_i - x_j|/p)}{l^2} - \frac{\|x_i - x_j\|^2}{2l^2}\right) \quad (25)$$

$$\frac{\partial k}{\partial A} = \exp\left(-\frac{(x_i - x_j)^2}{2l^2} - r^2 \sin^2\left(\frac{\pi(x_i - x_j)}{p}\right)\right) \quad (26)$$

$$\frac{\partial k}{\partial l} = A \frac{(x_i - x_j)^2}{l^3} \exp\left(-\frac{(x_i - x_j)^2}{2l^2} - r^2 \sin^2\left(\frac{\pi(x_i - x_j)}{p}\right)\right) \quad (27)$$

$$\frac{\partial k}{\partial r} = -2Ar \sin^2\left(\frac{\pi(x_i - x_j)}{p}\right) \exp\left(-\frac{(x_i - x_j)^2}{2l^2} - r^2 \sin^2\left(\frac{\pi(x_i - x_j)}{p}\right)\right) \quad (28)$$

$$\frac{\partial k}{\partial p} = \frac{2\pi Ar^2(x_i - x_j)}{p^2} \exp\left(-\frac{(x_i - x_j)^2}{2l^2} - r^2 \sin^2\left(\frac{\pi(x_i - x_j)}{p}\right)\right) \sin\left(\frac{\pi(x_i - x_j)}{p}\right) \cos\left(\frac{\pi(x_i - x_j)}{p}\right) \quad (29)$$

5.6 Details on the calculation of transit_length

We introduce a method to calculate **transit_length** that does not require prior knowledge of planetary parameters, such as the planetary radius (see [41]), but is purely based on the light curve. We start by defining the transit threshold $F_{\text{threshold}}$ as the flux level that is two standard deviations below the baseline flux observed outside of any transit (eq. (30)). This threshold helps to identify potential transit candidate points which are points where the flux $f(t)$ is less than or equal to the transit threshold $F_{\text{threshold}}$ (eq. (31)).

The ingress and egress times of the transit, marking the beginning and end of a transit event, are then determined by the earliest ((eq. (32)) and latest (eq. (33))) time points, respectively, at which the light curve falls below this threshold, making a transit event likely. Based on the ingress and egress, the transit duration can then be easily calculated (see eq. (10)).

$$F_{\text{threshold}} = F_{\text{notransit}} - 2 \times \sigma \quad (30) \quad T_{\text{candidate}} = f(t) \leq F_{\text{threshold}} \quad (31)$$

$$T_{\text{ingress}} = \min(T_{\text{candidate}}) \quad (32)$$

$$T_{\text{egress}} = \max(T_{\text{candidate}}) \quad (33)$$

5.7 Further Information on the Calculation of the Orbital Period

Whenever the orbital period a is calculated in AU units and we assume a negligibly small planetary mass in comparison to the star's mass, we can use a modified version of the Newton's version of Kepler's third law, justifying eq. (12)) (for further detail see: <https://www.austincc.edu/jheath/Solar/Hand/NVK3L/nvk3l.htm>, slide 12).

5.8 Celerite2

GPs often face computational challenges having a computational complexity of $O(N^3)$ where N is the dataset size resulting in an intractable likelihood evaluation for large datasets. Celerite addresses this by reducing the complexity to $O(NJ^2)$, such that it mainly depends on the number of J chosen terms which is typically much smaller than N . It achieves this by using a restricted class of covariance matrices that are sums of diagonal and semi-separable matrices.

We used celerite2 as a scalable alternative to regular GPs when fitting the large real astronomical time-series datasets to achieve results with limited computational capabilities and in a feasible amount of time. Specifically, we implemented a combination of two terms: one non-periodic and one quasi-periodic component (resembling the quasi-periodic (QP) kernel that we previously used for the GP fits on the simulated data). Celerite has been suggested as a suitable model to model astrophysical variability which has also motivated in the choice of incorporating it for our light curve data. We used the damped simple harmonic oscillator (SHO) term, which is recommended for most datasets and is defined by the power-spectrum density:

$$S(\omega) = \sqrt{\frac{2}{\pi}} \frac{S_0 \omega_0^4}{(\omega^2 - \omega_0^2)^2 + \omega_0^2 \omega^2 / Q^2} \quad (34)$$

This term is parametrised by the quality factor Q , the oscillator frequency ω_0 , and the amplitude variability S_0 . For further details on celerite, refer to the original paper by [17].